

# eBook on Biomedical Engineering

## Chapter 3

# Developing a Handheld Color Sensor Module to Monitor the Physiological Status of the Human Cardiovascular System in *Vivo*

Jung Y. Huang<sup>1\*</sup>; Chien-Yu Hsu<sup>2</sup>

<sup>1</sup>The T.K.B. Research Center for Photonics, Chiao Tung University, Hsinchu 300, Taiwan

<sup>2</sup>Department of Photonics, Chiao Tung University, Hsinchu 300, Taiwan

\*Correspondence to: Jung Y Huang, The T.K.B. Research Center for Photonics, Chiao Tung University, Hsinchu 300, Taiwan

Email: [jyhuang@faculty.nctu.edu.tw](mailto:jyhuang@faculty.nctu.edu.tw)

## Abstract

A sensitive color sensor module is developed to probe the physiological status of the human cardiovascular system. Breathing rhythm and heartbeat activity are observed in real time. The skin lightness and skin color expressed in the  $L^*a^*b^*$  color coordinate system fluctuate due to changes in blood perfusion according to the rhythm of the heartbeat. Using a Gaussian mixture model, the cardiovascular system is found to fall into three physiological states. The state distribution profiles differ before and after physical exercise. To obtain time-domain information from the color sensor data, we apply the hidden Markov model to retrieve the transition kinetics of the hidden states. Our data suggest that the cardiovascular system mainly resides in two of the three states and makes rare transitions to the third one under resting conditions. We speculate that this rare state may provide flexibility it needs to adapt to different physiological conditions.

**Keywords:** color sensor; photoplethysmography; heartbeat rate; blood volume pulse; principal component analysis; Gaussian mixture model; hidden Markov model

## 1. Introduction

The development of non-invasive methods to probe the human body *in vivo* remains a challenge in the biomedical field [1,2]. Blood volume pulse (BVP) and heartbeat rate (HR) have been established as useful supplemental indicators of cardiovascular health [3,4], stress and emotion [5,6,7], and exercise intensity [8,9], and have been used to monitor the progression of disease [10,11]. Plethysmography (PG), detection of cardiovascular pulse waves traveling through the body is usually performed by measuring variations in air pressure, impedance, or strain [12]. Photo-plethysmography (PPG) uses optical reflectance and is the least expensive method of implementing PG [13,14]. As blood exhibits greater light absorbance than its surrounding tissue, variations in blood volume are reflected by changes in light reflectance. A smaller blood volume generates greater optical reflectance and a higher PG signal [15]. The cardiovascular system continuously circulates blood around the human body. With each heartbeat, the blood circulation can create color variation in the skin, which allows BVP and HR to be measured remotely [16,17,18]. The non-contact photoplethysmographic monitoring of physiological parameters has been demonstrated by [17,19, 20] using low cost video camera in various lighting conditions [17]. Fast Fourier transform, independent component analysis (ICA), principal component analysis (PCA) [21], and brightness- and chrominance-based image processing techniques [17,20] have been developed to analyze color channels in facial regions in video recordings. An accurate PPG observation of HR and BVP against environmental change with low motion-induced artifacts has been achieved [20].

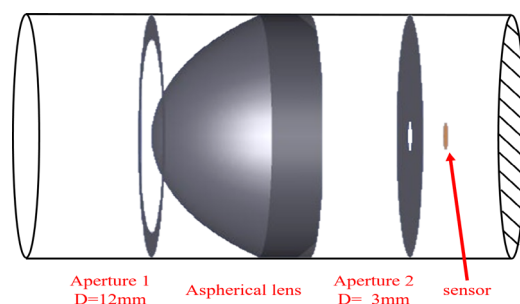
Recently, an algorithm named "Eulerian video magnification" developed to reveal the invisible signals in videos [22,23]. This technique uses a video sequence as an input, and the time series of color values at any pixel in a given frequency band of interest are amplified computationally. Temporal filtering can also be used at lower spatial frequencies to make a subtle input signal rise above the camera sensor and quantization noise. This allows the blood flow in the facial region to be detected and provides real-time pulse rate information [24].

Many novel algorithms and methodologies have been developed in biomedical engineering and other scientific domains. However, as previous studies have mainly focused on demonstrating the functionality of specific technique, certain critical issues remain understudied. For example, assuming that the human cardiovascular system is stochastically dynamic, is its physiological status appropriately described in a state space [25]? Can the relevant states in such a state space be described using HR and BVP? What are the unique features of those states? To answer these questions, we design and fabricate a handheld color sensor module to probe the physiological status of the human body *in vivo*. Our color sensor module can provide a clean waveform of breathing and heartbeat rhythm in real time. The color variations caused by breathing and the heartbeat occur along specific vectors in the RGB color space. The observed color variations for each heartbeat can be separated into changes in brightness and

chrominance. Different time delays relative to the electrocardiograph (ECG) are obtained for different regions of the body. Features extracted from the color variations reveal three distinct physiological states of the cardiovascular system. We use a Gaussian mixture model to deduce the distributions of the three states [26] and the hidden Markov model (HMM) with Gaussian emission distribution to determine the transition kinetics between the three states [27]. Our results show the cardiovascular system resides mainly in two of the three states under resting conditions, making rare transitions to the third state.

## 2 Experimental Procedure

### 2.1 Optical design of the color sensor module



#### ● Zemax optical signal simulation

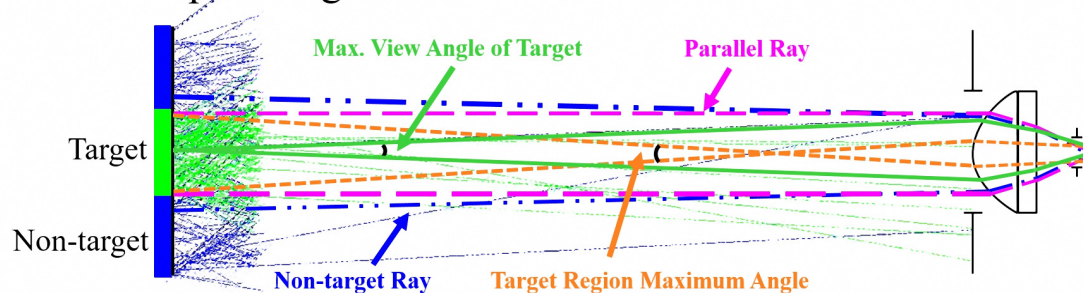


**Figure 1:** (Color online) Optical design of the color sensor module. (a) Schematic illustration of the light collection optics of the module. (b) Light tracing of the diffuse reflectance from the area to be observed (green) and nontargeted region (blue) based on Zemax simulation.

We design an optics for the color sensor module to enable it to efficiently collect the diffuse reflectance signal from the region of interest (ROI). This signal amounts to at least 50% of the total signal. We achieve this goal using quasi-telecentric optics [28]. An aspherical lens (ACL1512U, [29]) is positioned between a front (12-mm diameter) and back (3 mm) aperture, as illustrated in **Figure 1(a)**. **Figure 1(b)** presents the results of Zemax simulation under 500-lux normal indoor illumination. The simulation confirms that this optical design can deliver at least 54 lux to the sensor's active area. Of the received power, the signal from the ROI decreases only from 100% to 60% when the target-to-sensor distance increases from 4 cm to 10 cm.

## 2.2 Electronic design of the color sensor module

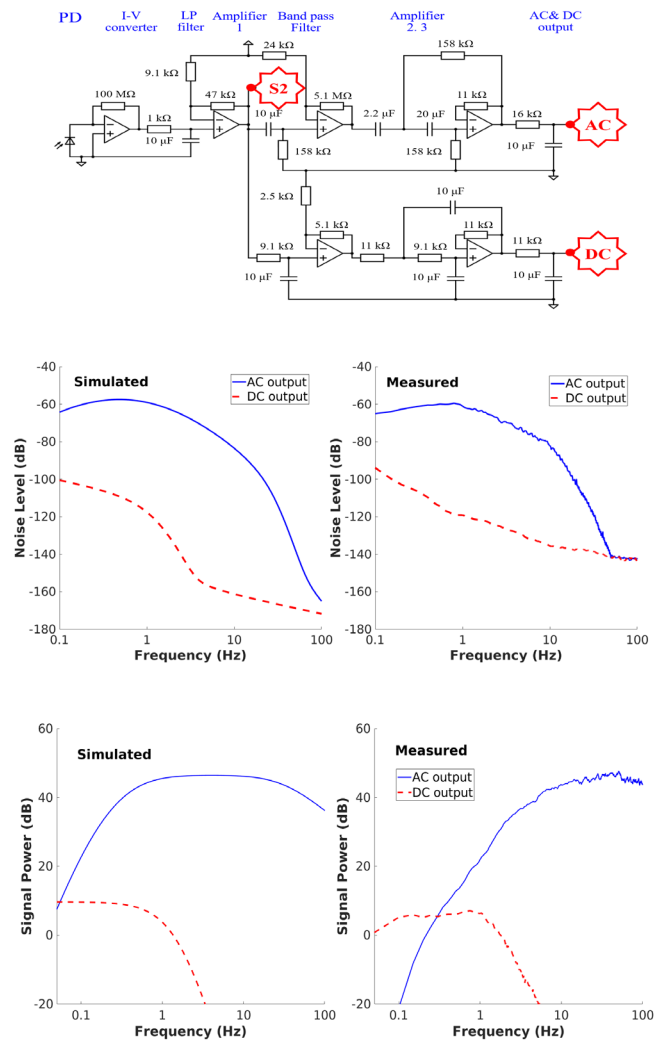


**Figure 2:** (Color online) Electronic design of the color sensor module. (a) Schematic of the electronic circuit for each color channel of the module. (b) Simulated (left) and measured (right) noise power spectra at AC and DC output highlighted in (a). (c) Simulated (left) and measured (right) signal amplification spectra at AC and DC output.

The diffuse reflectance signal is detected using a RGB color sensor (S9032, [30]) that can deliver a photocurrent of 9-20 nA at the RGB channels under 50 lux illuminance. A low-noise electronic circuit is designed and assembled to convert the photocurrent into voltage and route the voltage signals to AC and DC outputs.

**Figure 2(a)** shows the electronic circuit used for each color channel of the sensor module. The circuit can be divided into a current-to-voltage converter, preamplifier stage (S2), and AC and DC output stages. The AC channel provides a gain of 200 in a pass band of 0.1 Hz-28 Hz, which provides statistical information on the heartbeat. The DC channel amplifies the signal by 2 in a pass band of 0 Hz-1.6 Hz, and is designed to reveal color variations in the low frequency region.

**Figure 2(b)** presents the simulated and measured noise power spectra at the AC and DC output stages. The noise levels decay with increasing frequency (the cutoff effects of frequency filters in the circuit). The noise level in the pass band at the AC output is less than -60 dB, and can be lower than -100 dB to -120 dB at the DC output. The agreement is satisfactory. **Figure 2(c)** displays the simulated and measured gain spectra at the AC and DC outputs. The measured gain profiles match well with the simulated curves, indicating that this circuit can amplify the color signals with an acceptable S/N ratio for our research purpose.

The color sensor module provides six voltage signals at the AC and DC outputs. The electrical signals are converted to digital signals by a 24-Bit Delta-Sigma AD converter (ADS124S06, [31]) and stored in a computer or displayed in real time. To shorten the development time, we use an Arduino UNO developer board [32] with a C program to control the data acquisition. Typically, the sensor module is operated with a 100 Hz data acquisition cycle. Each cycle involves six cascading 1.6-ms AD conversions, which add up to a data conversion period of 9.6 ms.

## 2.3 Data processing method for the color sensing module

### 2.3.1 Color calibration















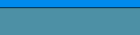
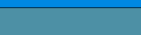


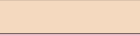
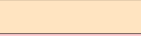






Different absorption properties of the vascularized dermis and bloodless epidermis layer result in observable color variations [33]. To measure color variation for physiological status monitoring, the module needs to be calibrated. The module generates six voltage values  $\vec{V}_{AC} = (V_{r,ac} V_{g,ac} V_{b,ac})^T$  and  $\vec{V}_{DC} = (V_{r,dc} V_{g,dc} V_{b,dc})^T$  at the AC and DC outputs with T denoting the transpose operation. Here, the voltage at the  $i = R, G, B$  channel is relevant to the photocurrent  $I_i$  by  $V_i = G_i I_i$ , with  $G_i$  denoting the effect from electronic amplification and frequency filter. The photocurrent is produced by an incident light  $L(\lambda)$  via  $I_i = \int L(\lambda) \cdot F_i(\lambda) d\lambda$  through a filter  $F_i(\lambda)$ . The resultant color coordinates (R G B) of the incident light  $L(\lambda)$  can then be determined as follows:

$$\begin{pmatrix} R \\ G \\ B \end{pmatrix} = \begin{pmatrix} C_r & 0 & 0 \\ 0 & C_g & 0 \\ 0 & 0 & C_b \end{pmatrix} \cdot \begin{pmatrix} V_r \\ V_g \\ V_b \end{pmatrix} + \begin{pmatrix} r_0 \\ g_0 \\ b_0 \end{pmatrix} \quad (1)$$

where  $C$  denotes the calibration matrix and  $(r_0 \ g_0 \ b_0)^T$  are the bias values in the RGB channels. The diagonal elements of the calibration matrix  $(C_i) = [V_i^w]^{-1}$  are determined by measuring  $\vec{V}^w = (V_r^w V_g^w V_b^w)^T$  on a standard white surface under the same lighting condition.

We use the reflected light from a standard white surface and specific color cards to calibrate the color sensor module. The measured values with a white light source with different illuminances are substituted into Eq. 1. The (R G B) obtained are compared with the known

color coordinates using an optimization solver. After the calibration, the sensor can directly read the color coordinates without needing to detrend and invert the data [15]. **Figure 3** shows the RGB readout values (right) and the known coordinates (left) for the set of colors. The agreement is satisfactory for skin color monitoring.

True RGB Coordinates		Readout values	
[ 255, 117, 107 ]			[ 255, 117, 107 ]
[ 255, 155, 55 ]			[ 255, 155, 55 ]
[ 255, 193, 0 ]			[ 255, 181, 19 ]
[ 255, 240, 43 ]			[ 255, 236, 51 ]
[ 180, 220, 66 ]			[ 255, 236, 51 ]
[ 0, 202, 132 ]			[ 8, 176, 125 ]
[ 0, 185, 243 ]			[ 19, 182, 255 ]
[ 0, 128, 236 ]			[ 0, 126, 223 ]
[ 66, 134, 156 ]			[ 66, 134, 156 ]
[ 231, 242, 251 ]			[ 234, 243, 255 ]
[ 243, 213, 184 ]			[ 255, 225, 186 ]
[ 241, 188, 200 ]			[ 255, 199, 204 ]
[ 243, 195, 189 ]			[ 255, 209, 202 ]

**Figure 3:** Measured RGB values (right) with the color sensor module and the known RGB color coordinates (left) of different color cards.

### 2.3.2 Signal processing procedure

The nonlocal mean algorithm (NLM) is a patch-based denoising method [34] that preserves signals and suppresses high-frequency noise. We use the NLM to clean up the high-frequency noises in our color signals. The denoised signal from the green DC channel is presented in **Figure 4(a)**. Breathing-induced color variations are visible. Specifically, inhaling (highlighted in red) yields higher color coordinates and exhaling (highlighted in green) yields lower color coordinates. These trends are consistent with the changes in oxygenated hemoglobin concentrations in the arterial blood associated with inhaling and exhaling.

Short segments of the AC signal (red) measured at the palm and in the ECG trace (black) are shown in **Figure 4(b)**. A good correlation between the color signal and ECG with a specific time delay is observed. A Fourier transform of a 120-min long color signal is presented in **Figure 4(c)**. A peak appearing at 0.2 Hz stems from the breathing activity. The main peak at 1.4 Hz can be attributed to the heartbeat rhythm. The remaining peaks at 2.8 Hz, 4.2 Hz, 5.6 Hz, and 7.1 Hz are the harmonics of the heartbeat. Up to fifth harmonics can be observed, indicating that the heartbeat-induced color waveform is precisely sampled by our color sensor module. Based on these findings, we conclude that skin color signals accurately reflect detailed information on cardiorespiratory activity.

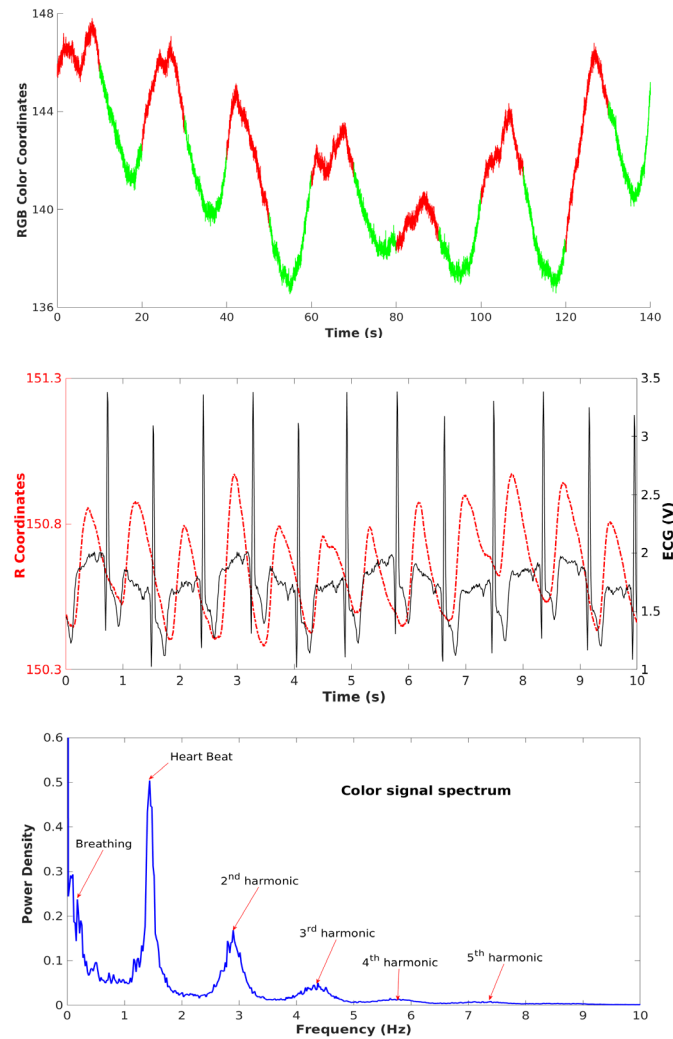


**Figure 4:** Measured output signals of the color sensor module. (a) DC output at the green channel showing correlation with the inhaling (red) and exhaling (green) air periods. (b) Measured AC signal at the palm from the red channel of the color sensor module and the ECG trace (black, for reference). (c) Fourier transform of a 120-min long blue AC signal measured at the palm.

To analyze the physiological states using the color sensor, we apply PCA to reduce the dimensionality of the RGB data. **Figure 5(a)** displays the RGB traces from the AC output. The first three PCA components are shown in **Figure 5(b)**. PC1 (in black), comprising 0.70 red, 0.43 green, and 0.31 blue, accounts for about 89% of the color variation. Similarly, the PC1 from the DC output accounts for 94% of the signal variation (data not shown) and is composed of 0.73 red, 0.50 green, and 0.33 blue. The color combination of PC1 reflects not only the skin tone but also the general physiological status of the test subjects.

The observed color variations caused by absorption differences between the arterial blood and bloodless skin layers can be better revealed along a specific vector in a normalized RGB-space. de Haan and van Leest [33] developed a procedure to extract the color vector for a given spectrum of light source and transfer characteristics of the optical filters used in the camera. Here we apply PCA to determine the color vectors based on the color variations caused by changes in cardiorespiratory activity.

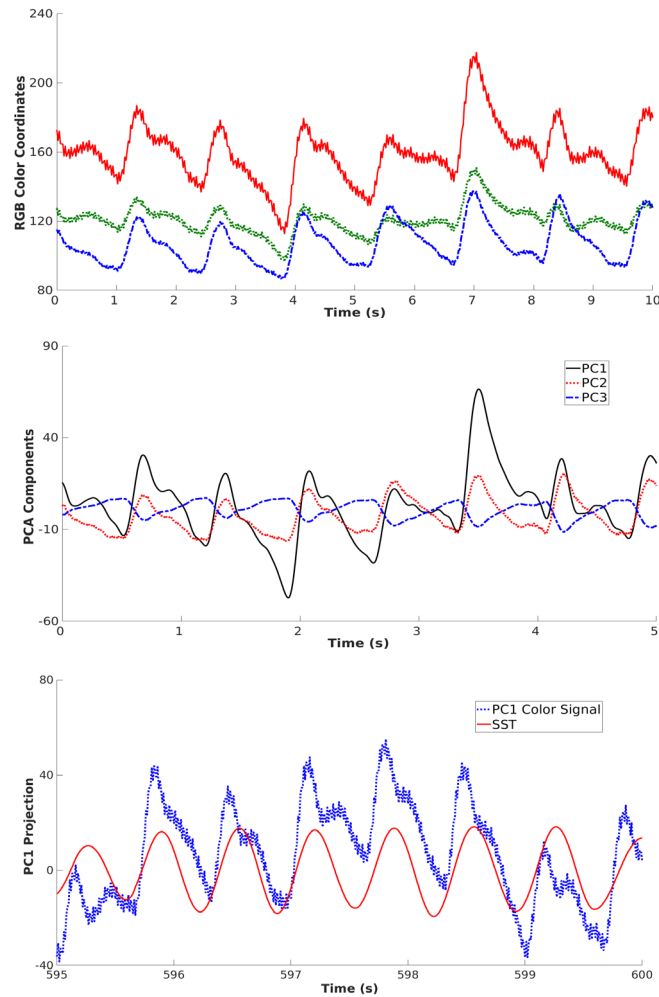


**Figure 5:** (a) AC signal traces of the color sensor module measured at the palm expressed in the CIE R (red) G (green) B (blue) color coordinates. (b) Corresponding PCA outputs (PC1: solid curve, PC2: dot, PC3: dash-dot) of the RGB traces shown in (a). (c) Synchro-squeezing transform results (red) of the PC1 (blue) of RGB color signals from the AC output.

The synchro-squeezing transform (SST), developed by Thakur, et al. [35], is a time-frequency signal analysis technique with the unique ability to identify and extract oscillatory components with time-varying frequencies and amplitudes. The algorithm is resistant to perturbations in the signal and Gaussian white noise. As our color signals exhibit a stochastic nature, with time-varying frequencies and amplitudes, we apply SST to select the signal of interest for further analysis. **Figure 5(c)** displays the effects of SST (in red) on the PC1 (in blue) of the AC signals. The color variations caused by heartbeat can be cleanly separated from the color variations caused by breathing rhythm without baseline drift. Thus, localizing the peak positions  $(t_j)_{j=1,\dots,N}$  and retrieving peak amplitudes  $(a_j)_{j=1,\dots,N}$  become more straightforward. From  $(t_j)_{j=1,\dots,N}$ , the heartbeat periods  $(\Delta t_j = t_{j+1} - t_j)_{j=1,\dots,N-1}$  can also be deduced.

### 3. Results and Discussion

#### 3.1. Heartbeat-induced color variations

Skin color signals are known to carry BVP information [15]. **Figure 6** shows the color signal from the green AC channel measured at various positions on the body. ECG, which



monitors the voltage changes caused by each heartbeat, gives us a convenient timing reference. Thus, during the color measurements, ECG is also recorded and displayed. The relative delay time is found to vary with locations, which reflects the cardiovascular pulse wave propagation delay from a neighboring artery to the measurement site [15].

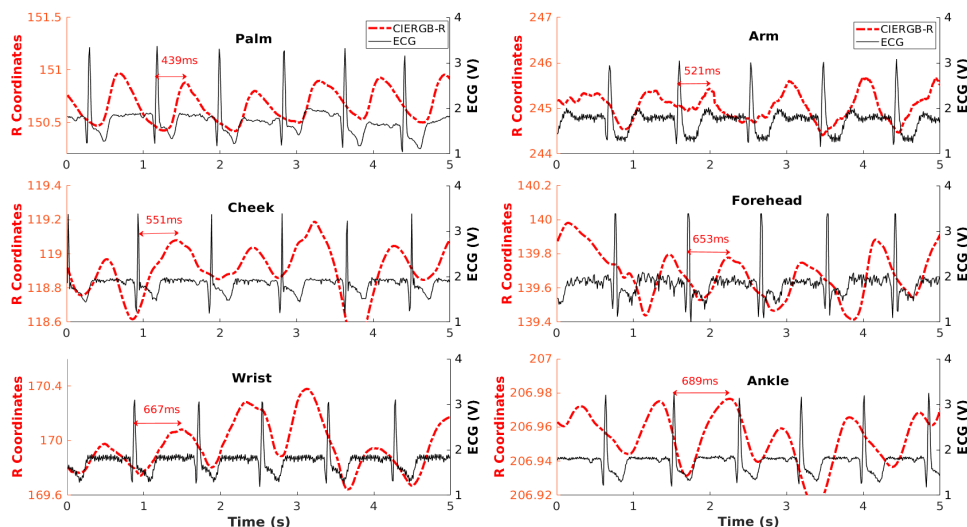


**Figure 6:** AC signal from the red channel of the color sensor module measured at the palm, arm, cheek, forehead, wrist, and ankle. ECG traces (black) are plotted as the timing reference.

### 3.2 Inter-heartbeat color variations

Although **Figure 6** displays distinctive variations in RGB coordinates, those signal variations can stem from changes in either lightness or colors. To solve this ambiguity, we convert the measured RGB coordinates to the CIELAB color system [36], which comprises lightness  $L^*$ , the red/green opposing colors  $a^*$ , and the yellow/blue opposing colors  $b^*$ . Note that a light color varying to green yields negative  $a^*$  values, whereas a light color varying to red gives a positive  $a^*$ . **Figure 7** presents the results and AC signal measured at the palm of a test subject. We find that most of the signal variations observed in RGB are indeed caused by  $L^*$  variations. The variation in  $a^*$  closely follows the variation in  $L^*$ . This similarity is understandable, as BVPs driven by the cardiovascular system can result in both lightness and red-green color variations. At the peaks of  $L^*$ ,  $a^*$  becomes redder. This observation agrees with the video recording result using the Eulerian video magnification algorithm [22,23]. However, the yellow/blue color variations along the  $b^*$  axis are somewhat irregular, suggesting that the physiological process that causes yellow/blue skin color variations may have a longer response time than the heartbeat. Therefore, as the two stochastic processes act together, the synchronization of the  $b^*$  signal with the ECG is destroyed quickly. We also find that the heartbeat feature disappears in the Fourier transform of  $b^*$ .

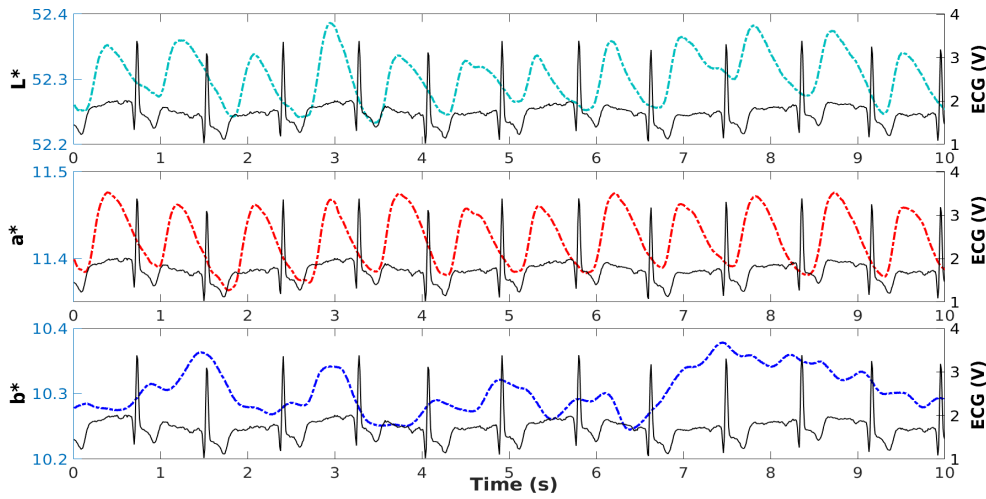


**Figure 7:** An AC signal trace (red) of the color sensor module measured at the palm is expressed in the  $L^*a^*b^*$  color coordinates ( $L^*$ : top,  $a^*$ : middle,  $b^*$ : bottom). ECG traces (black) are plotted as the timing reference.

### 3.3 Probability distribution of the physiological states of the human cardiovascular system

The color variation amplitudes  $(a_j)_{j=1,\dots,N}$  and heartbeat periods  $(\Delta t_j)_{j=1,\dots,N}$  of a 120-min long PC1 signal from both the AC and DC channels are determined and used to label the physiological states embedded in the color signal. The data are fitted to GMMs with different numbers of Gaussian components ( $N$ ). The corresponding Bayesian information criterion (BIC) [37] index is calculated. In **Figure 8**, the inverse BIC is plotted against  $N$ . Our results indicate that using a three-component GMM is the best way of addressing fitting errors and the overfitting problem in this context.

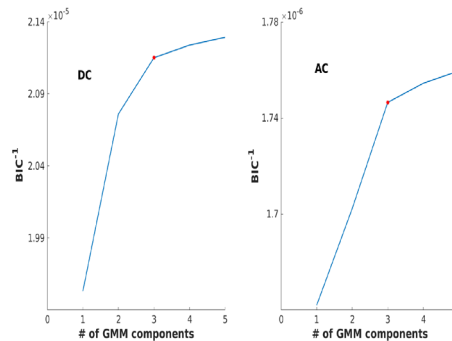


**Figure 8:** BIC index plotted as a function of the number of Gaussian components ( $N$ ). A 120-min PC1 signal trace from either (a) the DC or (b) the AC channel of the color sensor module is fitted to a GMM with different  $N$  values.

The GMM provides the distribution of the three states on the plane of  $a_j$  and  $\Delta t_j$ . **Figure 9(a)** displays the probability distribution estimated from the PC1 data sequence from the DC channel. The data are collected over 6 days (1 hr each day). The total number of breathing cycles in the data set is about 2,160. The breathing period in the state highlighted in red is centered at 10 s, whereas the two other states have either longer (blue) or shorter (green) breathing cycles. The breathing period of the green state is about half of that of the red state, and the green state shows weaker color variations. In contrast, compared with the red state, the blue state represents deep breathing with a larger amplitude of color variation, and possibly

more oxygen dissolved in the arterial blood.

In **Figure 9(b)**, the distribution of  $a_j$  and  $\Delta t_j$  extracted from the AC PC1 signal is displayed. The total number of heartbeats in this data set is about 29,000. The heartbeat period of the test subject at rest lies in a 0.6-0.8 s range. Different amplitudes of color variation are found for the three states. The state labeled in blue stems from a rarer heartbeat activity, whose period is widely distributed and reveals the smallest color variation. The green state has a heartbeat period of 0.75 s, which is similar to that of the red state (0.7 s), but has a wider  $\Delta t_j$  distribution. Of the three states, the  $\Delta t_j$  distribution appears to be more tightly regulated in the red state than in the other two states.

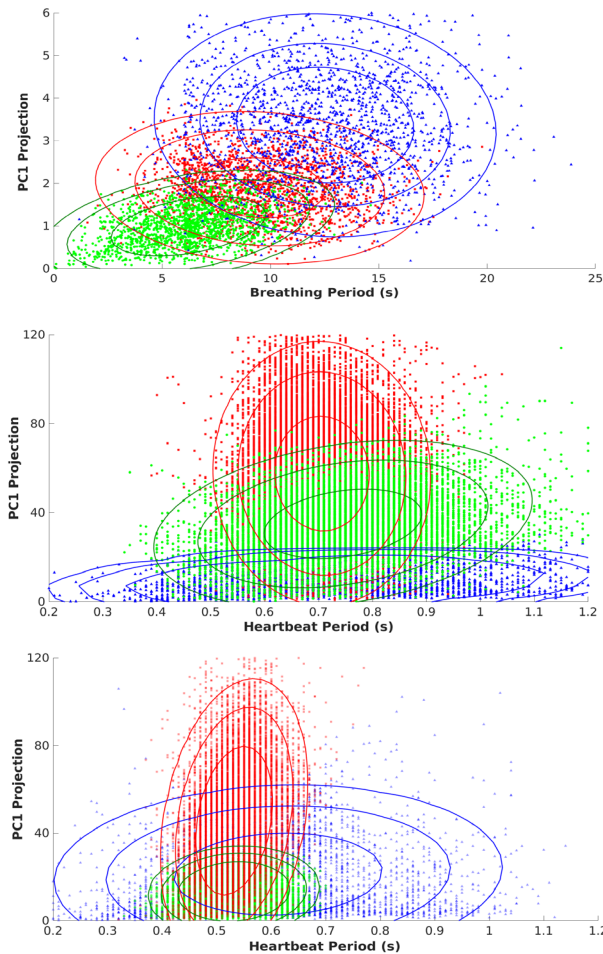


**Figure 9:** A 120-min PC1 signal trace measured at the palm with the color sensor module fitted to GMM of  $N=3$  (coded by red, green, and blue). The signal trace from (a) DC, (b) AC (at rest), and (c) AC (physical exercise).

How do the physiological states of the cardiovascular system respond to a physical exercise? To answer this question, we apply the color sensor to the same test subject after physical exercise. The resulting distribution of  $a_j$  and  $\Delta t_j$  is displayed in **Figure 9(c)**. We notice that the peaks of the red and green state distributions shift down to  $\Delta t_j = 0.53$  s, correlating with an increased cardiovascular output. A narrower distribution profile along  $\Delta t_j$  is also observed in the green state. Interestingly, the blue state is more widely distributed on  $a_j$ . Our data indicate that the cardiovascular system makes the heartbeat periods of the red and green states shorter and skews toward the blue state as a response to exercise for increasing oxygen supply to the body.

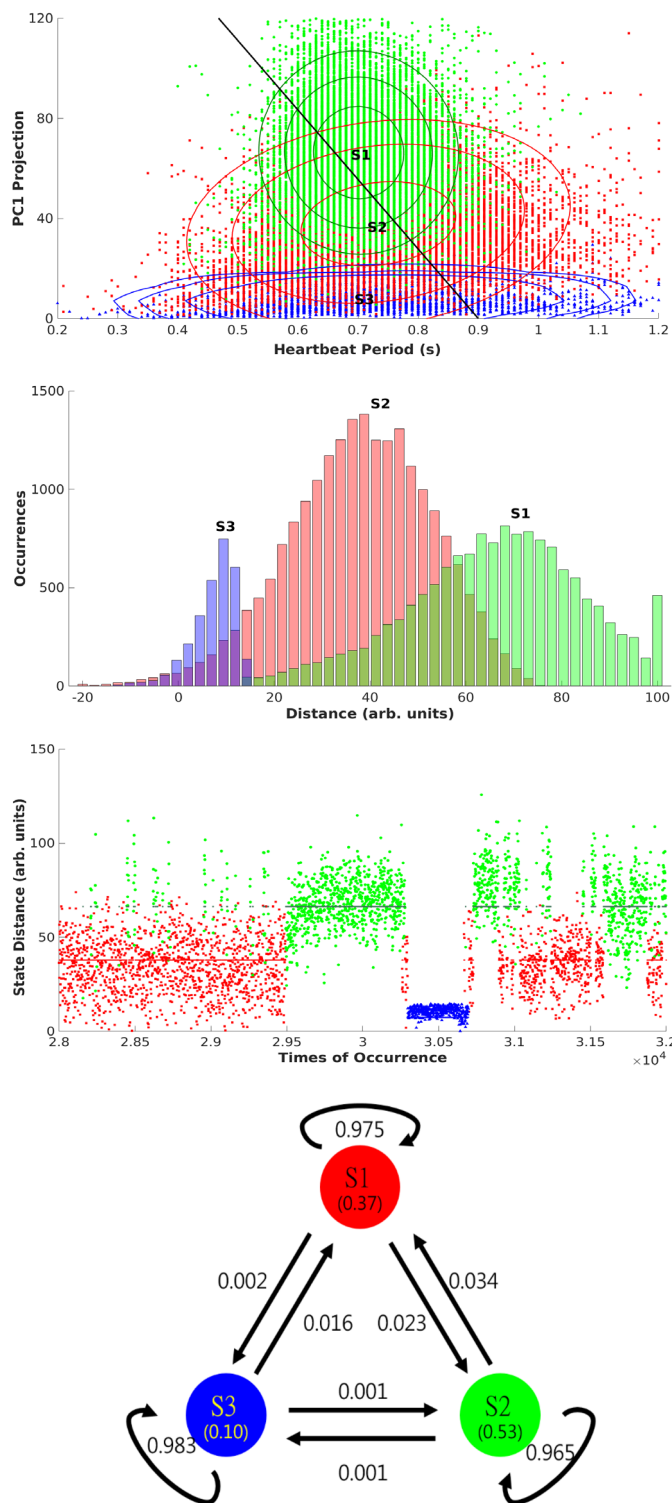


**Figure 10:** (a) A 120-min PC1 signal trace (measured at the palm) taken from the AC output of the color sensor module is fitted to the hidden Markov model with three hidden states (coded as red (S1), green (S2), and blue (S3)). The black line is a projection of the data points. (b) Histograms of the three hidden states along the black projection line. (c) Transition kinetics plotted with respect to their times of occurrence. (d) The hidden state transition diagram collected from a 120-min long sequence.

### 3.4 Revealing transition kinetics of physiological states with hidden Markov model

Although a GMM can yield distributions of physiological states, time-domain information is missing. Does the cardiovascular system switch rapidly between the three states or remain trapped in one or two states, only rarely making state transitions? To retrieve such time-domain information from our measurements, we fit PC1 traces of the AC channel to a Gaussian hidden Markov model (gHMM) [38]. This is done by first preparing the model parameters, which include initial population probabilities for each hidden state, transition probabilities, and the means and covariance matrix of the Gaussian emission probabilities. The results of GMM analysis and a randomly generated transition probability matrix are used as the initial model parameters. We then refine these model parameters using the expectation-maximization algorithm for the measured PC1 data. Finally, a forward-backward algorithm is invoked to predict the hidden state sequence with the observed PC1 data sequence and refined model parameters. The predicted probability distributions of the hidden state population are presented in **Figure 10(a)**. The highest probability values of the heartbeat period are found to be 0.75 s for S1 and 0.7 s for S2. S2 has a larger color variation amplitude than S1, whereas S3 exhibits the lowest color variation across a wide heartbeat period. The black line provides a projection of the data points. The histograms of inline distances for each state are shown in **Figure 10(b)**. The metric of inline distance provides a higher-resolution account of the transition kinetics. In **Figure 10(c)**, the inline distances of 4,000 data sequences are plotted against the times of occurrence. The hidden state transition kinetics collected from a 360-min long sequence are summarized in **Figure 10(d)**.

Our data suggests that the stochastic dynamics of the cardiovascular system can be described in a state space span by the features  $a_j$  and  $\Delta t_j$ . The occupation probabilities of S1 (red), S2 (green), and S3 (blue) are found to be 0.37, 0.53, and 0.1, respectively. The cardiovascular system appears to reside in the S1 or S2 states for most of the time, occasionally transitioning to S3 ( $<0.002$ ). Although a robust biological system is usually tightly regulated, it may possess the flexibility needed to adapt and survive in different physiological conditions. Our data suggest that S3 may represent such a cardiovascular state in this context.

## 4. Conclusion

In summary, we have developed a sensitive color sensor module to study the physiological status of the human cardiovascular system. This handheld portable module reveals both breathing and heartbeat rhythms in real time based on color variations in the skin. The measured color variation amplitudes also yield blood volume pulse information for each heartbeat. The color variations expressed in the  $L^*a^*b^*$  color coordinate system resolve the variations that stem from heartbeat-induced lightness changes and perfusion-induced color changes in the skin. Different delay times are observed in different regions of the body, depending on the

distance between the measurement location and the neighboring artery. Three physiological states of our cardiovascular system are discovered using the color sensor module. Detailed probability distributions of the states are retrieved using GMM, showing different mean values and covariance matrix for the different states. The distribution profiles also differ significantly before and after physical exercise. The hidden Markov model is used to retrieve the transition kinetics of the hidden states. The results reveal that the cardiovascular system resides mainly in S1 and S2; rarely in S3. We reason that the latter state may provide the cardiovascular system with the freedom it needs to adapt to conditions that demand a rapid increase in cardiovascular output.

## 5. Acknowledgement

This research is funded by the Ministry of Science and Technology of the Republic of China (grant number MOST 106-2112-M-009-019-MY3).

## 6. References

1. A. M. Scholz, L. Bunger, J. Kongsro, U. Baulain, and A. D. Mitchell, "Non-invasive methods for the determination of body and carcass composition in livestock: dual-energy x-ray absorptiometry, computed tomography, magnetic resonance imaging and ultrasound: invited review," *Animal* 9(7), 1250-1264 (2015).
2. X. Garcia, L. Mateu, J. Maynar, J. Mercadal, A. Ochagava, and A. Ferrandiz, "Estimating cardiac output. utility in the clinical practice. available invasive and non-invasive monitoring," *Medicina Intensiva* 35(9), 529-592 (2011).
3. G. Tanaka, K. Yamakoshi, Y. Sawada, K. Matsumura, K. Maeda, Y. Kato, M. Horiguchi, and H. Ohguro, "A novel photoplethysmography technique to derive normalized arterial stiffness as a blood pressure independent measure in the finger vascular bed," *Physiol Meas.* 32(11), 1869-1883 (2011).
4. J. T. Kuvin, A. R. Patel, K. A. Sliney, N. G. Pandian, J. Sheffy, R. P. Schnall, R. H. Karas, and J. E. Udelson, "Assessment of peripheral vascular endothelial function with finger arterial pulse wave amplitude," *Am. Heart J.* 146(1), 168-174 (2003).
5. M. Hamer, G. Tanaka, H. Okamura, A. Tsuda, and A. Steptoe, "The effects of depressive symptoms on cardiovascular and catecholamine responses to the induction of depressive mood," *Biological Psychology* 74(1), 20-25 (2007).
6. R. J. McNally, N. B. Lasko, S. A. Clancy, M. L. Macklin, R. K. Pitman, and S. P. Orr, "Psychophysiological responding during script-driven imagery in people reporting abduction by space aliens," *Psychol. Sci.* 15(7), 493-497 (2004).
7. K. Matsumura, T. Yamakoshi, H. Noguchi, P. Rolfe, and Y. Matsuoka, "Fish consumption and cardiovascular response during mental stress," *BMC Res. Notes* 5, 288-296 (2012).
8. K. Matsumura, T. Yamakoshi, Y. Yamakoshi, and P. Rolfe, "The effect of competition on heart rate during kart driving: A field study," *BMC Res. Notes* 4, 342-346 (2011).
9. T. Yamakoshi, K. Matsumura, Y. Yamakoshi, H. Hirose, and P. Rolfe, "Physiological measurements and analyses in motor sports: a preliminary study in racing kart athletes," *European Journal of Sport Science* 10(6), 397-406 (2010).
10. I. M. Lin, S. Y. Fan, Y. H. Lu, C. S. Lee, K. T. Wu, and H. J. Ji, "Exploring the blood volume amplitude and pulse transit time during anger recall in patients with coronary artery disease," *J. Cardiology* 65(1), 50-56 (2015).
11. M. Elgendi, "On the analysis of fingertip photoplethysmogram signals," *Curr. Cardiol. Rev.* 8(1), 14-25 (2012).

12. C. P. Criea, S. Sorichter, H. J. Smith, P. Kardos, R. Merget, D. Heise, and D. Berdel, "Body plethysmography: principles and clinical use," *Respiratory Medicine* 105, 959-971 (2011).
13. A. B. Hertzman and C. R. Spealman, "Observations on the finger volume pulse recorded photoelectrically," *Am. J. Physiol.* 119, 334-335 (1937).
14. J. Allen, "Photoplethysmography and its application in clinical physiological measurement," *Physiol. Meas.* 28(3), R1-R39 (2007).
15. A. A. Kamshilin and N. B. Margaryants, "Origin of photoplethysmographic waveform at green light," *Physics Procedia*. 86, 72-80 (2017).
16. Y. Sun, "Photoplethysmography revisited: from contact to noncontact, from point to imaging," *IEEE Trans. Biomed. Eng.* 63(3), 463-477 (2016).
17. W. Verkruyse, L. O. Svaasand, and J. S. Nelson, "Remote plethysmographic imaging using ambient light," *Opt. Express* 16(26), 21434-21445 (2008).
18. M. Kumar, A. Veeraraghavan, and A. Sabharwal, "DistancePPG: Robust non-contact vital signs monitoring using a camera," *Biomed. Opt. Express* 6(5), 1565-1588 (2015).
19. M. Z. Poh, D. J. McDuff, and R. W. Picard, "Advancements in noncontact, multiparameter physiological measurements using a webcam," *IEEE Trans. Biomed. Eng.* 58(1), 7-11 (2011).
20. G. de Haan and V. Jeanne, "Robust pulse rate from chrominance-based rPPG," *IEEE Trans. Biomed. Eng.* 60(10), 2878-2886 (2013).
21. C. Wang, T. Pun, and G. Chanel, "A comparative survey of methods for remote heart rate detection from frontal face videos," *Front. Bioeng. Biotechnol.* 6, a33 (2018).
22. H. Y. Wu, M. Rubinstein, E. Shih, J. V. Guttag, F. Durand, and W. T. Freeman, "Eulerian video magnification for revealing subtle changes in the world," *ACM Trans. Graph* 31(4), a65 (2012).
23. N. Wadhwa, H. Y. Wu, A. Davis, M. Rubinstein, E. Shih, G. J. Mysore, J. G. Chen, O. Buyukozturk, J. V. Guttag, W. T. Freeman, and F. Durand, "Eulerian video magnification and analysis," *Comm. of ACM* 60(1), 87-95 (2017).
24. A. Al-Naji, S. H. Lee, and J. Chahl, "An efficient motion magnification system for real-time applications," *Machine Vision and Applications* 29, 585-600 (2018).
25. K. P. Murphy, *Machine Learning: A Probabilistic Perspective* (Chap. 18) (The MIT Press, Cambridge, Massachusetts, USA, 2012) pp. 631-660.
26. K. P. Murphy, *Machine Learning: A Probabilistic Perspective* (Chap. 11) (The MIT Press, Cambridge, Massachusetts, USA, 2012) pp. 337-373.
27. K. P. Murphy, *Machine Learning: A Probabilistic Perspective* (Chap. 17) (The MIT Press, Cambridge, Massachusetts, USA, 2012) pp. 589-628.
28. G. H. Chen and J. Y. Huang, "Development of a hyperspectral imaging technique with internal scene scan for analysing the chemistry of food degradation," *J. Spectral Imaging* 7, a12 (2018).
29. Thorlab, "Aspheric Condenser Lens," (2019), <https://www.thorlabs.com/thorproductfm?partnumber=ACL1512U-A>.
30. Hamamatsu, "RGB color sensor," (2019), [https://www.hamamatsu.com/resources/pdf/ssd/s9032-02\\_kspd1067e.pdf](https://www.hamamatsu.com/resources/pdf/ssd/s9032-02_kspd1067e.pdf).
31. Texas Instruments, "Delta-Sigma ADC," (2019), <http://www.ti.com/product/ADS124S06>.

32. Arduino, "Arduino UNO developer board," (2019), [https://en.wikipedia.org/wiki/Arduino\\_Uno](https://en.wikipedia.org/wiki/Arduino_Uno).
33. G. de Haan and A. van Leest, "Improved motion robustness of remote-PPG by using the blood volume pulse signature," *Physiol Meas.* 35(9), 1913-1926 (2014).
34. B. Tracey and E. Miller, "Nonlocal means denoising of ECG signals," *IEEE Trans. Biomed. Eng.* 59(9), 2382-2386 (2012).
35. G. Thakur, E. Brevdo, N. S. Fukar, and H. T. Wu, "The synchrosqueezing algorithm for time-varying spectral analysis: robustness properties and new paleoclimate applications," *Signal Processing* 93, 1079-1094 (2013).
36. WikiPedia, "CIELAB color space," (2019), [https://en.wikipedia.org/wiki/CIELAB\\_color\\_space](https://en.wikipedia.org/wiki/CIELAB_color_space).
37. T. Huang, H. Peng, and K. Zhang, "Model selection for gaussian mixture models," *Statistica Sinica* 27, 147-169 (2017).
38. S. Paris, "EM for HMM multivariate Gaussian processes," (2019), <https://www.mathworks.com/matlabcentral/fileexchange/20712-em-for-hmm-multivariate-gaussian-processes>.